Online Parameter Adjustment Method for Arm Voltage Estimation of the Modular Multilevel Converter

Abel A. Taffese, *Student Member, IEEE,* Erik de Jong, Salvatore D'Arco,
and Elisabetta Tedeschi, *Senior Member, IEEE,*

Abstract—The method used to calculate insertion indexes plays an important role in determining the overall performance of the Modular Multilevel Converter (MMC). Direct voltage control, which is the simplest option, results in a large circulating current ripple because this modulation technique does not account for the arm voltage ripples. This led to the development of compensated modulation techniques that compensate for the arm voltage ripples thereby eliminating the circulating current ripple. There are two variants of compensated modulation: closed-loop and open-loop. The closed-loop version requires measurement of the arm voltages without distortion and delay, which is difficult to achieve in practice. The open-loop method overcomes this challenge by using estimated arm voltages. However, accurate knowledge of the system parameters is needed for effective removal of the circulating current ripples. This is a limitation because the parameters change with time and operating conditions. This paper presents a modified version of the open-loop method, which includes a scheme for correcting parameter errors online. The method estimates the parameters, the arm capacitances and time delay, by using feedback controllers acting on the circulating current ripples. Mathematical derivation of the method, together with its validation using simulation and experimental tests, is presented in detail.

Index Terms—MMC, parameter correction, open-loop, compensated modulation, parameter estimation, capacitance, time delay

I. INTRODUCTION

THE Modular Multilevel Converter (MMC) has a complex structure with large number of Sub-Modules (SMs) and interconnections [1], [2]. Thus, it requires a number of additional controllers [3]–[5] compared to the two level Voltage Source Converter (VSC). One of these added controllers is responsible for the calculation of insertion indexes, which are signals that dictate the percentage of SMs inserted in a given arm at a given time. Several methods to calculate these indexes have been described in literature [6]–[11], each one leading to a different trade-off between simplicity and performance. The simplest option is the direct voltage control (a subset of uncompensated modulation techniques [11]), which assumes

Abel A. Taffese and Elisabetta Tedeschi are with the Department of Electric Power Engineering, Norwegian University of Science and Technology, Trondheim, Norway (e-mail: abel.taffese@ntnu.no and elisabetta.tedeschi@ntnu.no)

Erik de Jong is with the Electrical Energy Systems group, Eindhoven University of Technology, Eindhoven, The Netherlands (email: E.C.W.de.Jong@tue.nl)

Salvatore D'Arco is with the Department of Energy Systems, SINTEF Energy Research, Trondheim, Norway (email: salvatore.darco@sintef.no)

that the arm capacitor voltages are ripple-free, and hence, it generates the ac and common-mode references without applying any compensation. This leads to a significant amount of second harmonic ripple in the circulating current, resulting in an increased power loss [12]. Moreover, direct voltage control leads to an uncontrolled coupling between the different harmonic components, which can lead to oscillations during transients [13]. Circulating current suppression controllers [7], [14]–[17] have been proposed to suppress the ripple, but the oscillation problem [13] is not solved by such controllers. Furthermore, it was found that these controllers can negatively interact with other higher level controllers [18].

Compensated modulation [11] (also referred to as indirect modulation [3]) solves the aforementioned problems by avoiding the need for a circulating current suppression controller. This is achieved by dividing the voltage references, generated by the high-level controllers, by the respective arm voltages to generate the insertion indexes. By doing so, the circulating current ripple can be effectively suppressed without any additional controller [12]. Applying compensated modulation also limits the coupling among the internal variables of the MMC [11], avoiding the undesired oscillations reported in [13]. The arm voltage can be either measured (closed-loop [12]) or estimated (open-loop [6]) for the purpose of compensated modulation.

The main drawbacks of compensated modulation using measured arm voltages are that the system becomes open-loop unstable [19], and that ideal measurement of the arm voltage is required to achieve effective suppression of the ripple. The first drawback can be overcome by implementing closed-loop control of the sum and difference energy components in a leg. However, the second problem is difficult to address because measurement systems will inevitably exhibit distortion and delay. The open-loop method solves these two problems by using estimated values of the arm voltages. Furthermore, it has been shown in [20], [21] that the open-loop approach is globally asymptotically stable without a closed-loop arm voltage controller. However, it requires accurate knowledge of the parameters, particularly the arm capacitance and time delay due to measurement and communication. Such a requirement is not easy to satisfy because, even if the parameters are accurately known in the beginning, their values are likely to change as the components age and as the environmental conditions change. For example, capacitance of capacitors can drop by up to $20\,\%$ over their lifetime [22], [23]. This leads to a mismatch between the actual parameters and the ones known

to the arm voltage estimator. Such a mismatch will be referred to as *'parameter error'* henceforth.

The effect of parameter errors is twofold: 1) the average arm energy deviates from the desired reference because of capacitance error, and 2) the ripples in the arm energy are phase shifted and scaled due to capacitance and time delay errors, leading to circulating current ripple. The first effect, in the extreme case, causes the converter to go into over-modulation, even when the value set by the open-loop modulator is within the normal operation range. Ref. [9] overcomes this problem by controlling the average arm energy using the average value of the measured arm voltage, while the ripples are estimated using measured currents and references from high level controllers. This is possible because the average part is not significantly affected by distortion and delay of the measurement path. Although the method in [9] makes the average part insensitive to parameter errors, effective removal of the circulating current ripple still requires accurate knowledge of the arm capacitance value and of the time delay in the measurement and control path. This paper proposes a complete scheme, based on [9], that includes a method for correcting parameter errors online. The proposed method uses the first and second harmonic components (with respect to the fundamental ac side frequency) of the circulating current ripple as feedback. These current components should not be present if the parameters are accurately known. Therefore, the proposed method is a feedback controller that adjusts the estimated parameters to force these two circulating current components to zero. Unlike circulating current suppression controllers, this controller is activated only when the circulating current ripple magnitude exceeds a preset threshold and then deactivated once the parameter correction is done. Additionally, the proposed controller can be designed to be significantly slower (10 to 100 times) compared to other controllers leading to sufficient frequency decoupling. This frequency separation is not applicable in circulating current suppression controllers because they have be tuned to be sufficiently fast to keep the circulating current ripple close to zero by actively rejecting disturbances coming from other controllers and changes in operating point. Consequently, the proposed controller can be designed not to negatively interact with other controllers in the system. A similar scheme using closed loop controllers to compensate for arm inductor parameter variation in the energy balancing of the alternate arm converter has been reported in recent literature [24].

The main contributions of this paper are: 1) mathematical derivation of the relation between the parameter errors and the circulating current ripples, and 2) development of a method to correct the errors online using a feedback controller. The method has been validated by using simulations and experimental tests. The remainder of this paper is organized as follows. Section II presents an average model of the MMC. The arm voltage estimation method adopted in this paper is dealt with in Section III. The effect of parameter errors, together with the proposed parameter correction method, is discussed in Section IV. Simulation and experimental results are addressed in Section V, followed by conclusion in Section VI.

II. AVERAGE MODEL OF THE MMC

The MMC can be modeled with different levels of detail depending on the type of study and size of the system [11], [25]–[30]. This study focuses on the dynamics and the parameter variation effects at the arm level, which are shown to be adequately represented by average models [25], [31]. Sub-Module level individual parameter variations are not considered because the collective effect of such variations is captured by an aggregate arm level variation, which is sufficient for the purpose of this paper. Therefore, an average modeling approach is adopted in this paper. Circuit diagram of a leg of an MMC is depicted in Fig. 1 together with relevant variable definitions and the assumed polarities. Two current loops can be identified from the circuit. The first one is the ac current loop encompassing the grid voltage, the transformer, the arm inductors, and the equivalent ac voltage of the arms. The other one is the dc loop, which is formed by the dc voltage (capacitance), the arm voltages, and the arm inductors. All the quantities in this paper are in per-unit (pu) with respect to the base values given in Table I, where the ac base values are applied to the quantities along the ac loop while the dc ones are used for variables in the dc loop. The arm voltages and currents are considered to be dc side quantities. The pu base value for the energy, W_b in Table I, is chosen such that the relation between voltage across an arm, v, and energy of the arm, w, becomes $w = v^2$ in per-unit [31]. The model presented in this paper closely follows [25] and [31] with some differences because of the per-unit base values chosen in this paper. The upper and lower arm insertion indexes, n_u and n_l are calculated as depicted in (1). The sub-scripts u and l denote the upper and lower arms, respectively. The superscript $(\cdot)^r$ indicates reference values generated by the controllers.

$$
\begin{aligned}
n_u &= \frac{1}{\hat{v}_{cu}} \left(\frac{1}{2} v_{dc}^r - v_c^r - \frac{1}{2} v_s^r \right) \\
n_l &= \frac{1}{\hat{v}_{cl}} \left(\frac{1}{2} v_{dc}^r - v_c^r + \frac{1}{2} v_s^r \right)
\end{aligned}
\tag{1}
$$

where v_{dc}^r is the dc voltage reference, v_c^r is a control signal used to shape the circulating current, and v_s^r is the ac voltage reference. $\hat{v}_{cu}$ and $\hat{v}_{cl}$ are estimates of the arm voltages whose values are selected based on the method used for calculating the insertion indexes. For example, the dc voltage is used in the case of direct voltage control [12] while measured arm voltages (sum of capacitor voltages) are used in compensated modulation [11].

Estimates of the arm voltages [6] are used in this paper. The upper and lower arm currents, Fig. 1, can be decomposed into common mode, i_c, and differential mode, i_s, components as shown in (2). This decomposition helps in separating the controllers of the ac side from those of the dc side.

$$
\begin{aligned}
i_u &= i_c + \frac{2}{3} i_s \\
i_l &= i_c - \frac{2}{3} i_s
\end{aligned}
\tag{2}
$$

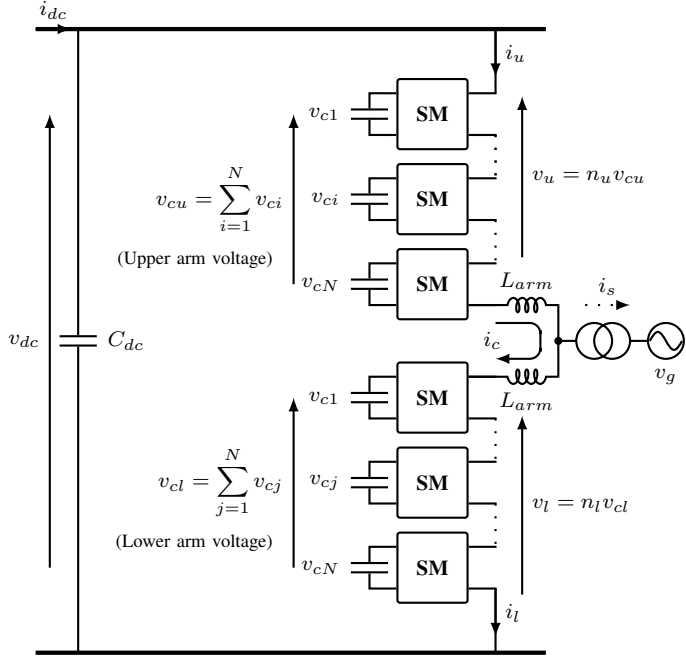The factor 2/3 is a result of the selected per-unit conversion (Table III). The energy in the upper and lower arms,

Fig. 1: Per phase MMC circuit.

TABLE I: per-unit base value definitions.

Description	Value
power	S_b
dc voltage	V_b^{dc}
ac voltage	$V_b^{ac} = \frac{1}{2} V_b^{dc}$
dc current	$I_b^{dc} = S_b / V_b^{dc}$
ac current	$I_b^{ac} = \frac{2}{3} S_b / V_b^{ac}$
dc resistance	$R_b^{dc} = V_b^{dc} / I_b^{dc}$
ac resistance	$Z_b^{ac} = V_b^{dc} / I_b^{dc}$
dc inductance	$L_b^{dc} = R_b^{dc}$
dc capacitance	$C_b^{dc} = 1 / R_b^{dc}$
arm energy	$W_b = \frac{1}{2} C_{SM} / N \left(V_b^{dc} \right)^2$
per-unit dc inductance	$l_{dc} = L_{arm} / L_b^{dc}$
per-unit dc resistance	$r_{dc} = R_{arm} / Z_b^{dc}$
per-unit arm capacitance	$C_{arm} = c_a C_b^{dc} = C_{SM} / N$

Equations (4) and (5) constitute a third order dynamic model that will be used in this paper.

III. ESTIMATION OF THE ARM VOLTAGES

The ripple in the arm voltages can be estimated from the measured currents, and reference voltages obtained from the controllers. The implementation presented in [25] uses closed-form expressions of per-phase ripple estimates. Alternative methods have been presented in [7], [32], which include a method that extracts the ripples from the measured arm voltages using band-pass filters [7]. This approach is attractive from the perspective of minimizing computation and avoiding nonlinear operations [7]. The implementation in this paper is based on the closed-form expressions [25] because the same equations will be used in the derivation of the algorithm for parameter error correction in Section IV. However, the results obtained in this paper are equally applicable to the band-pass filter approach. The following assumptions [6] are made to simplify the derivation:

A.1 The ac voltages and currents are purely sinusoidal waveforms at fundamental frequency. Additionally, the grid frequency is assumed to be constant over time, which implies that all the harmonic components are also constant frequency.

A.2 The dc quantities and peak values of the ac quantities change slowly compared to the fundamental period. Consequently, they are treated as constants in the derivation.

A.3 The estimated arm capacitor voltages converge to the actual values in steady-state (i.e. $\hat{v}_{cu,l} = v_{cu,l}$)

Assumption **A.1** is reasonable because the MMC is capable of producing near-sinusoidal waveforms. Moreover, it can be shown that the impact of harmonics in the ac quantities on the arm voltage estimator is negligible under normal operating conditions where the THD is low (for example below $1.5\,\%$ according to IEEE 519 [33]). The second assumption is not valid during fast transients, but this does not have a significant impact; its effect will be shown using simulation

w_u and w_l, are governed by (3).

$$
\begin{aligned}
\frac{c_u}{2} \frac{\mathrm{d}}{\mathrm{dt}} w_u &= v_{cu} \cdot n_u \cdot i_u \\
&= \frac{v_{cu}}{\hat{v}_{cu}} \left(\frac{1}{2} v_{dc}^r - v_c^r - \frac{1}{2} v_s^r \right) \left(i_c + \frac{2}{3} i_s \right) \\
\frac{c_l}{2} \frac{\mathrm{d}}{\mathrm{dt}} w_l &= v_{cl} \cdot n_l \cdot i_l \\
&= \frac{v_{cl}}{\hat{v}_{cl}} \left(\frac{1}{2} v_{dc}^r - v_c^r + \frac{1}{2} v_s^r \right) \left(i_c - \frac{2}{3} i_s \right)
\end{aligned}
\tag{3}
$$

where c_u and c_l are the upper and lower arm capacitances in pu. Equation (3) can be transformed into the form shown in (4) where the upper and lower energy terms are replaced by their sum, $w^\Sigma = w_u + w_l$, and difference, $w^\Delta = w_u - w_l$, and the common mode voltage is defined as $v_{cm}^r = (v_{dc}^r - 2v_c^r)/2$.

$$
\begin{aligned}
\frac{1}{2} \frac{\mathrm{d}}{\mathrm{dt}} w^\Sigma &= \left(\frac{v_{cu}}{c_u \hat{v}_{cu}} + \frac{v_{cl}}{c_l \hat{v}_{cl}} \right) \left(v_{cm}^r i_c - \frac{1}{3} v_s^r i_s \right) \\
&+ \left(\frac{v_{cu}}{c_u \hat{v}_{cu}} - \frac{v_{cl}}{c_l \hat{v}_{cl}} \right) \left(\frac{2}{3} v_{cm}^r i_s - \frac{1}{2} v_s^r i_c \right) \\
\frac{1}{2} \frac{\mathrm{d}}{\mathrm{dt}} w^\Delta &= \left(\frac{v_{cu}}{c_u \hat{v}_{cu}} - \frac{v_{cl}}{c_l \hat{v}_{cl}} \right) \left(v_{cm}^r i_c - \frac{1}{3} v_s^r i_s \right) \\
&+ \left(\frac{v_{cu}}{c_u \hat{v}_{cu}} + \frac{v_{cl}}{c_l \hat{v}_{cl}} \right) \left(\frac{2}{3} v_{cm}^r i_s - \frac{1}{2} v_s^r i_c \right)
\end{aligned}
\tag{4}
$$

Dynamics of the circulating current can similarly be derived as shown in (5).

$$
\begin{aligned}
l_{dc} \frac{\mathrm{d}}{\mathrm{dt}} i_c &= \frac{1}{2} v_{dc} - \frac{1}{2} \left(\frac{v_{cu}}{\hat{v}_{cu}} + \frac{v_{cl}}{\hat{v}_{cl}} \right) v_{cm}^r \\
&+ \frac{1}{4} \left(\frac{v_{cu}}{\hat{v}_{cu}} - \frac{v_{cl}}{\hat{v}_{cl}} \right) v_s^r - r_{dc} i_c
\end{aligned}
\tag{5}
$$

where l_{dc} and r_{dc} are the arm inductance, L_{arm}, and resistance, R_{arm}, in pu with the dc base values in Table I.

TABLE II: Definition of harmonic components.

Time Domain	Phasor
$h_{10} = \int \left(\frac{2}{3} v_{cm}^r i_s - \frac{1}{2} v_s^r i_{c0}\right) dt$	$\vec{\mathbf{H}}_{10} = \frac{2}{j3\omega} v_{cm}^r \vec{\mathbf{I}}_s - \frac{1}{j2\omega} \vec{\mathbf{V}}_s^r i_{c0}$
$h_{20} = -\frac{1}{3} \int v_s^r i_s \, dt$	$\vec{\mathbf{H}}_{20} = -\frac{1}{j12\omega} \vec{\mathbf{V}}_s^r \vec{\mathbf{I}}_s$
$h_{11} = \int v_{cm}^r i_{c1} \, dt$	$\vec{\mathbf{H}}_{11} = \frac{1}{j\omega} v_{cm}^r \vec{\mathbf{I}}_1$
$h_{21} = -\frac{1}{2} \int v_s^r i_{c1} \, dt$	$\vec{\mathbf{H}}_{21} = -\frac{1}{j8\omega} \vec{\mathbf{V}}_s^r \vec{\mathbf{I}}_1$
$h_{12} = -\frac{1}{2} \int v_s^r i_{c2} \, dt$	$\vec{\mathbf{H}}_{12} = -\frac{1}{j4\omega} \vec{\mathbf{V}}_s^{r*} \vec{\mathbf{I}}_2$
$h_{22} = \int v_{cm}^r i_{c2} \, dt$	$\vec{\mathbf{H}}_{22} = \frac{1}{j2\omega} v_{cm}^r \vec{\mathbf{I}}_2$
$h_{32} = -\frac{1}{2} \int v_s^r i_{c2} \, dt$	$\vec{\mathbf{H}}_{32} = -\frac{1}{j12\omega} \vec{\mathbf{V}}_s^r \vec{\mathbf{I}}_2$

and experimental results in Section V. Assumption **A.2** is acceptable because the grid quantities are assumed not to change abruptly under normal operation. Assumption **A.3** is affected by the presence of parameter errors and will be discussed in Section IV. The phase voltage reference and current are given by (6) where V_s^r and I_s are peak values of the phase voltage reference and phase current, respectively. The quantities ϕ_v and ϕ_i are phase angle offsets of the voltage and current, respectively, with respect to a common angle reference. For the case of a balanced three phase system, phases b and c would have additional phase shifts of $-2\pi/3$ and $2\pi/3$, respectively.

$$v_s^r = V_s^r \cos\left(\omega t + \phi_v\right)$$
$$i_s = I_s \cos\left(\omega t + \phi_i\right) \tag{6}$$

Since all the ac components in the system have constant frequency and amplitude in steady-state (assumption **A.1** and **A.2**), they can be converted into complex constants, at their respective frequencies, in phasor domain. Phasor form is chosen because it makes the derivation applicable to both single phase and balanced three-phase systems. For balanced three phase systems, these phasors correspond to the *dq* values where the *d* and *q* components are the real and imaginary parts, respectively. The phasors will be denoted by boldface capital letters with arrows on top.

Because of assumption **A.3** the energy dynamics given by (4) simplifies to (7).

$$\frac{\mathrm{d}}{\mathrm{d}t} w^\Sigma = 2b^\Sigma \left(v_{cm}^r i_c - \frac{1}{3} v_s^r i_s\right)$$
$$+ 2b^\Delta \left(\frac{2}{3} v_{cm}^r i_s - \frac{1}{2} v_s^r i_c\right)$$
$$\frac{\mathrm{d}}{\mathrm{d}t} w^\Delta = 2b^\Delta \left(v_{cm}^r i_c - \frac{1}{3} v_s^r i_s\right)$$
$$+ 2b^\Sigma \left(\frac{2}{3} v_{cm}^r i_s - \frac{1}{2} v_s^r i_c\right) \tag{7}$$

where $b^\Sigma = \left(\frac{1}{c_u} + \frac{1}{c_l}\right)$ and $b^\Delta = \left(\frac{1}{c_u} - \frac{1}{c_l}\right)$. It should be noted that (7) can still be used when there are parameter errors because the effect of the mismatch between the estimates, $\hat{v}_{cu,l}$, and the actual arm voltages, $v_{cu,l}$, has a negligible impact on the energy dynamic equations. This can be verified by linearizing the divisions in (4) and evaluating the contribution

of the mismatches. Consequently, (7) is used in the remainder of this paper. Depending on the harmonic content in i_c, different components appear in w^Σ and w^Δ. In this paper the circulating current is assumed to have a dc component, i_{c0}, a first harmonic, i_{c1}, and a second harmonic, i_{c2}. The other harmonic components are not included because their magnitudes are assumed to be negligible compared to the aforementioned components. As a result, w^Σ and w^Δ can be written in the form shown in (8) by expanding the ac components in (7).

$$w^\Sigma = 2b^\Sigma \left(h_{20} + h_{11} + h_{22}\right)$$
$$+ 2b^\Delta \left(h_{10} + h_{12} + h_{21} + h_{32}\right) + 2w^0$$
$$w^\Delta = 2b^\Delta \left(h_{20} + h_{11} + h_{22}\right)$$
$$+ 2b^\Sigma \left(h_{10} + h_{12} + h_{21} + h_{32}\right) \tag{8}$$

where h_{kp} is the kth harmonic energy component caused by the pth harmonic of i_c. For instance, h_{21} is a second harmonic component due to the first harmonic of i_c (i_{c1}). Table II shows the definitions of the harmonic components together with their corresponding phasors. $\vec{\mathbf{V}}_s^r$ and $\vec{\mathbf{I}}_s$ are the ac voltage reference and ac current in phasor form. v_{cm}^r and i_{c0} are assumed to be dc quantities, so the notation for these quantities does not change when transforming to phasor form.

The phasor equations in Table II are obtained by transforming the terms in the brackets of (7) into phasor form followed by time-integration, which, in phasor domain, is equivalent to division by $jk\omega$ where k is the harmonic order. Products of two time-domain sinusoids such as $v_s^r i_s$ are expanded using the trigonometric angle addition formula before conversion to phasor form (i.e. $v_s^r i_s = \frac{1}{2} V_s^r I_s \left(\cos(\phi_v - \phi_i) + \cos(2\omega t + \phi_v + \phi_i)\right)$, which translates to a dc component, $\frac{1}{2}\Re\{\vec{\mathbf{V}}_s^r \vec{\mathbf{I}}_s^*\}$, and a second harmonic phasor, $\frac{1}{2}\vec{\mathbf{V}}_s^r \vec{\mathbf{I}}_s$).

Equation (8) and Table II describe a general case where the circulating current has non-zero ripple, which happens only when there are parameter errors. This will be revisited in Section IV. However, for the purpose of deriving the arm voltage estimator equations, the parameters are assumed to be known, which means that there is no circulating current ripple. This implies that all the harmonics due to the first and second harmonic components of the circulating current are zero (i.e. $h_{11} = h_{21} = h_{12} = h_{22} = h_{32} = 0$). Hence, the estimates of the sum and difference energies, $\hat{w}^\Sigma$ and $\hat{w}^\Delta$, can be written in the form shown in (9).

$$\hat{w}^\Sigma = 2w^0 + 2\hat{b}^\Sigma \hat{h}_{20} + 2\hat{b}^\Delta \hat{h}_{10}$$
$$\hat{w}^\Delta = 2\hat{b}^\Sigma \hat{h}_{10} + 2\hat{b}^\Delta \hat{h}_{20} \tag{9}$$

where $\hat{h}_{10}$ and $\hat{h}_{20}$ are the first and second harmonic components, respectively, in time domain. w^0 is the average (dc) component, $\hat{b}^\Sigma$ and $\hat{b}^\Delta$ the arm capacitance parameters known to the estimator. Phasor domain representation of $\hat{h}_{10}$ and $\hat{h}_{20}$

are $\hat{\vec{H}}_{10}$ and $\hat{\vec{H}}_{20}$, respectively, which are defined in (10).

$$\hat{\vec{H}}_{10} = \frac{1}{j\omega} \left(\frac{2}{3} v_{cm}^r \vec{I}_s - \frac{1}{2} i_{c0} \vec{V}_s^r \right)$$

$$\hat{\vec{H}}_{20} = \frac{-1}{12j\omega} \vec{V}_s^r \vec{I}_s \tag{10}$$

The corresponding time-domain ripples, $\hat{h}_{10}$ and $\hat{h}_{20}$, are obtained by inverse transforming (10). For the case of balanced three-phase systems, this is done by applying dq to abc transformations at fundamental frequency for $\hat{\vec{H}}_{10}$, and at second-harmonic for $\hat{\vec{H}}_{20}$. Since $\hat{\vec{H}}_{20}$ is a negative sequence signal, phases b and c of the output of the second harmonic transformation should be swapped. Then, the sum and difference energies are computed using (9). Finally, the arm voltages are computed from the corresponding energy term as shown in (11).

The complete structure of the arm voltage estimator, together with the average energy controller, for a balanced three-phase system is shown in Fig. 2. Although the system is balanced with respect to the ac current and voltages, the estimator parameters, $\hat{b}^\Sigma$ and $\hat{b}^\Delta$, should be computed per phase since the capacitance of the arms can be different because of tolerance values.

$$\hat{v}_{cu} = \sqrt{\hat{w}_u} = \sqrt{\frac{\hat{w}^\Sigma + \hat{w}^\Delta}{2}}$$

$$\hat{v}_{cl} = \sqrt{\hat{w}_l} = \sqrt{\frac{\hat{w}^\Sigma - \hat{w}^\Delta}{2}} \tag{11}$$

The average (dc) component of $\hat{w}^\Sigma$ can be obtained by averaging of the arm voltages at the leg level (per-phase) or converter level. Since the converter is assumed to be symmetric, converter level averaging is used. Therefore, the measured dc energy, w_m^0 in Fig. 2, is obtained by averaging the six arm energies as given by (12). This effectively extracts the average value from the measurement. Then a low-pass filter is applied to the signal to remove noise, distortion, and fast transients. The measured dc circulating current, i_{c0m} in Fig. 2, is obtained by averaging the arm current as shown in (12).

$$w_m^0 = \frac{1}{6} \sum_{x,y} v_{cxy}^2 \quad i_{c0m} = \frac{1}{6} \sum_{x,y} i_{xy} \tag{12}$$

$$\text{where} \quad x \in \{u, l\} \quad and \quad y \in \{a, b, c\}$$

The average energy is controlled in closed-loop using cascaded controllers with an inner current-loop. The controllers are designed using modulus and symmetric optimum techniques [34]. Additionally, a compensation for the delay of the energy filter, w_{comp}, proposed in [9] was applied to improve the controller response. In addition to removing noise from the measurements, the filters in Fig. 2 also serve the purpose of limiting the response speed of the controllers so that their performance becomes less sensitive to variations in the measurement and communication delay in the system. For instance, the current filter time-constant was chosen in such a way that it is five times the worst case anticipated time delay in the current measurement path, which is set to be $100\,\mu s$.

The choice is a compromise between robustness to delay variation, and speed of response. Therefore, any variation in the measurement delay will not necessitate retuning of the controllers as long as it is below the worst case bound.

IV. PARAMETER ERROR CORRECTION

This section presents a method that automatically corrects parameter errors by monitoring second harmonic ripple in the circulating current. First, the derivation of the relation between the circulating current and the parameter errors will be presented. The main parameters that are not known or that can change over time are the arm capacitances, and the communication and measurement delays between the controller and the converter. Capacitance values change over time because of environmental stress and aging [22]. The time delay, denoted by t_d, accounts for communication delays, filter lags, and any delay introduced when sampling analog signals. The derivation will be based on the circulating current dynamic equation, (5).

Any difference between the estimated and the actual arm voltages results in circulating current ripples. The right-hand side of (5) is a nonlinear function of the arm voltages because of the divisions of the arm voltages by their respective estimates. In order to simplify the analysis, these equations can be linearized assuming that the ripple is a small percentage of the average arm voltage. This is achieved by using (13), which is derived by assuming that the upper and lower arm energies are balanced at a steady state operating point ($W^0 = \hat{W}^0$).

$$\frac{v_{cu/l}}{\hat{v}_{cu/l}} = \sqrt{\frac{w_{u/l}}{\hat{w}_{u/l}}}$$

$$\approx \frac{1}{2W^0} \left[w_{u/l} - \hat{w}_{u/l} \right] + 1 \tag{13}$$

After substituting (13) into (5) and transforming to the Σ and Δ energy terms, the circulating current dynamics becomes the one given by (14).

$$l_{dc} \frac{\mathrm{d}}{\mathrm{dt}} i_c = \frac{1}{2} v_{dc} - v_{cm}^r - r_{dc} i_c$$

$$- \frac{1}{4W^0} \left[\left(w^\Sigma - \hat{w}^\Sigma \right) v_{cm}^r \right.$$

$$\left. - \frac{1}{2} \left(w^\Delta - \hat{w}^\Delta \right) v_s^r \right] \tag{14}$$

Equation (14) shows that i_c can be split into two components: a component purely due to the control signal v_{cm}^r, and a component also influenced by estimation errors, $w^\Sigma - \hat{w}^\Sigma$ and $w^\Delta - \hat{w}^\Delta$. The control signal v_{cm}^r does not normally include harmonics; therefore, any harmonic component in i_c is due to the estimator error. The first and second harmonics of i_c will be derived in this section. Since the procedure is similar for both harmonics, the derivation of the second harmonic is presented, while the results are summarized for the first harmonic. The second harmonic component of i_c, i.e. i_{c2}, is related to the second harmonic of the sum energies, and the first and third harmonics of the difference energies. This can be confirmed by substituting these values in (14). The dynamics of i_{c2} is given
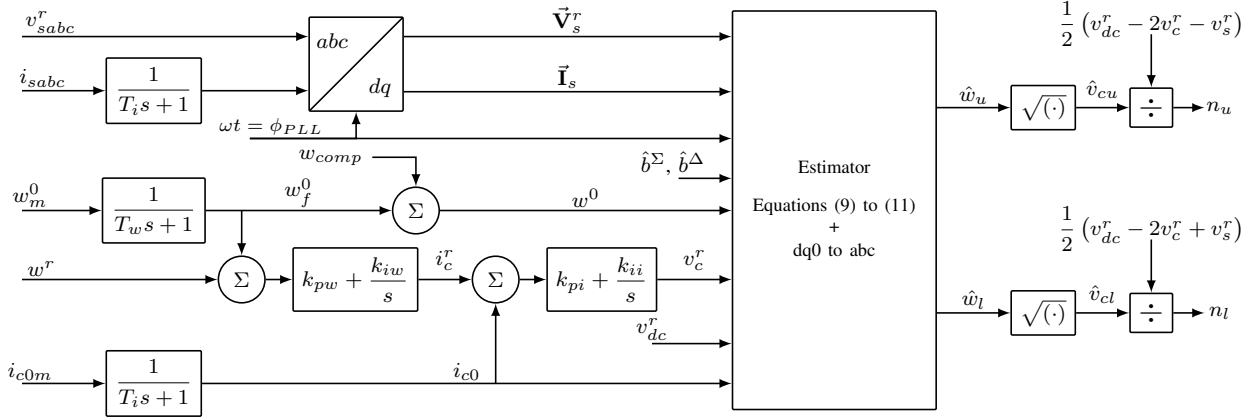
Fig. 2: Block diagram of the arm voltage estimation method with average energy control.

by (15), which is obtained by substituting the arm energies from (8) and (9) into (14).

$$l_{dc}\frac{\mathrm{d}}{\mathrm{dt}}i_{c2} + r_{dc}i_{c2} = -\frac{1}{2W^0}\left[v_{cm}^r\left(b^\Sigma h_{20} + b^\Sigma h_{22}\right.\right.$$
$$\left.+ b^\Delta h_{21} - \hat{b}^\Sigma \hat{h}_{20}\right) - \frac{1}{2}v_s^r\left(b^\Delta h_{11} + b^\Sigma h_{10}\right) \quad (15)$$
$$\left.+ b^\Sigma h_{12} + b^\Sigma h_{32} - \hat{b}^\Sigma \hat{h}_{10}\right)\right]$$

Grouping the terms common to both the estimator and the actual values, leads to (16).

$$l_{dc}\frac{\mathrm{d}}{\mathrm{dt}}i_{c2} + r_{dc}i_{c2} = -\frac{1}{2W^0}\left[b^\Delta\left(v_{cm}^r h_{21} - \frac{1}{2}v_s^r h_{11}\right)\right.$$
$$+ b^\Sigma\left(v_{cm}^r h_{22} - \frac{1}{2}v_s^r(h_{12} + h_{32})\right)$$
$$\left.+ v_{cm}^r\left(b^\Sigma h_{20} - \hat{b}^\Sigma \hat{h}_{20}\right) - \frac{1}{2}v_s^r\left(b^\Sigma h_{10} - \hat{b}^\Sigma \hat{h}_{10}\right)\right]$$
$$(16)$$

The third line of (16) is related to the estimation errors while the first part is due to a combination of the harmonics in the actual values. After converting (16) into phasor form, substituting the harmonic values from Table II, and grouping like terms, (17) is obtained.

$$-(R + jX_2)\vec{\mathbf{I}}_2 = v_{cm}^r\left(b^\Sigma\vec{\mathbf{H}}_{20} - \hat{b}^\Sigma\hat{\vec{\mathbf{H}}}_{20}\right)$$
$$- \frac{1}{4}\vec{\mathbf{V}}_s^r\left(b^\Sigma\vec{\mathbf{H}}_{10} - \hat{b}^\Sigma\hat{\vec{\mathbf{H}}}_{10}\right)$$
$$- jG_{22}\vec{\mathbf{I}}_2 + j\vec{\mathbf{G}}_{21}\vec{\mathbf{I}}_1 \quad (17)$$
$$\text{where} \quad G_{22} = \frac{b^\Sigma}{\omega}\left[\frac{1}{2}(v_{cm}^r)^2 + \frac{1}{12}\|\vec{\mathbf{V}}_s^r\|^2\right]$$
$$\vec{\mathbf{G}}_{21} = \frac{3b^\Delta}{8\omega}v_{cm}^r\vec{\mathbf{V}}_s^r$$

where $R = 2W^0 r_{dc}$ and $X_2 = 4W^0\omega l_{dc}$. $\|\cdot\|$ is the magnitude (norm) operator. A similar equation for the first harmonic component, i_{c1}, is derived by following the same reasoning and approach, as shown in (18). The relevant energy harmonics, for the first harmonic current, are the first harmonic component of the sum energies and the second harmonic

components of the difference energies.

$$-(R + jX_1)\vec{\mathbf{I}}_1 = v_{cm}^r\left(b^\Delta\vec{\mathbf{H}}_{10} - \hat{b}^\Delta\hat{\vec{\mathbf{H}}}_{10}\right)$$
$$- \frac{1}{4}\vec{\mathbf{V}}_s^{r*}\left(b^\Delta\vec{\mathbf{H}}_{20} - \hat{b}^\Delta\hat{\vec{\mathbf{H}}}_{20}\right)$$
$$- jG_{11}\vec{\mathbf{I}}_1 + j\vec{\mathbf{G}}_{12}\vec{\mathbf{I}}_2 \quad (18)$$
$$G_{11} = \frac{b^\Sigma}{\omega}\left[(v_{cm}^r)^2 + \frac{1}{32}\|\vec{\mathbf{V}}_s^r\|^2\right] \quad \vec{\mathbf{G}}_{12} = \frac{3b^\Delta}{8\omega}v_{cm}^r\vec{\mathbf{V}}_s^{r*}$$

where $X_1 = 2W^0\omega l_{dc}$. Comparing (17) and (18), it can be noted that $\vec{\mathbf{I}}_2$ is related to the mismatch between b^Σ and $\hat{b}^\Sigma$, while $\vec{\mathbf{I}}_1$ is related to the mismatch between b^Δ and $\hat{b}^\Delta$. For example, with the parameters used in this paper (Table III), and at full load condition, a 10% deviation common to both the upper and lower arms leads to $\|\vec{\mathbf{I}}_2\| = 5.4\,\mathrm{A}$ (6.3% in pu) and $\|\vec{\mathbf{I}}_1\| = 0.09\,\mathrm{A}$ (0.01% in pu). Similarly, a 10% differential deviation between the upper and lower arms leads to $\|\vec{\mathbf{I}}_2\| = 0.15\,\mathrm{A}$ (0.18% in pu) and $\|\vec{\mathbf{I}}_1\| = 3.8\,\mathrm{A}$ (4.4% in pu).

A. The Effect of Time Delay

Time delay affects the actual and estimated phasor quantities differently. The actual values are affected through the ac reference v_s^r (see (7)), which is delayed by t_d before reaching the arms. The estimator, on the other hand, accesses the references without delay since it resides in the controller, but the estimates themselves, $\hat{v}_{cu}$ and $\hat{v}_{cl}$, are delayed by t_d when they propagate as part of the insertion indexes. Therefore, the delay is applied to only v_s^r for the actual values while it is applied to all the quantities in the estimates. Time delay in phasor domain is represented by multiplication with $\mathrm{e}^{-jk\phi_d}$ where k is the harmonic order and $\phi_d = \omega t_d$ is the phase shift at fundamental frequency. The phasor quantities on the right-hand side of (17) and (18) can, therefore, be expanded as shown in (19) for the actual values and in (20) for the estimates.

$$\vec{\mathbf{H}}_{10} = \frac{1}{j\omega}\left[\frac{2}{3}v_{cm}^r\vec{\mathbf{I}}_s - \frac{1}{2}i_c^0\vec{\mathbf{V}}_s^r\mathrm{e}^{-j\phi_d}\right]$$
$$\vec{\mathbf{H}}_{20} = -\frac{1}{j12\omega}\vec{\mathbf{I}}_s\vec{\mathbf{V}}_s^r\mathrm{e}^{-j\phi_d} \quad (19)$$

$$\hat{\vec{\mathbf{H}}}_{10} = \frac{1}{j\omega}\left[\frac{2}{3}v_{cm}^r\vec{\mathbf{I}}_s - \frac{1}{2}i_c^0\vec{\mathbf{V}}_s^r\right]\mathrm{e}^{\text{-}j\phi_d}$$
$$\hat{\vec{\mathbf{H}}}_{20} = -\frac{1}{j12\omega}\vec{\mathbf{I}}_s\vec{\mathbf{V}}_s^r\mathrm{e}^{\text{-}2j\phi_d} \tag{20}$$

After substituting these phasor quantities into (17) and (18) and simplifying, (21) and (22) are obtained.

$$-(R+jX_2)\vec{\mathbf{I}}_2 = -jG_{22}\vec{\mathbf{I}}_2 + j\mathrm{e}^{\text{-}j\phi_d}\vec{\mathbf{G}}_{21}\vec{\mathbf{I}}_1$$
$$\frac{j}{4\omega}\left[v_{cm}^r\vec{\mathbf{I}}_s\left(b^\Sigma\mathrm{e}^{j\phi_d} - \hat{b}^\Sigma\right)\right.$$
$$\left. - \frac{1}{2}i_{c0}\vec{\mathbf{V}}_s^r\left(b^\Sigma - \hat{b}^\Sigma\right)\right]\vec{\mathbf{V}}_s^r\mathrm{e}^{\text{-}2j\phi_d} \tag{21}$$

$$-(R+jX_1)\vec{\mathbf{I}}_1 = -jG_{11}\vec{\mathbf{I}}_1 + j\mathrm{e}^{j\phi_d}\vec{\mathbf{G}}_{12}\vec{\mathbf{I}}_2$$
$$-\frac{j}{\omega}\left[\left(\frac{2}{3}(v_{cm}^r)^2 + \frac{1}{48}\|\vec{\mathbf{V}}_s^r\|^2\right)\vec{\mathbf{I}}_s\left(b^\Delta\mathrm{e}^{j\phi_d} - \hat{b}^\Delta\right)\right.$$
$$\left. - \frac{1}{2}v_{cm}^r i_{c0}\vec{\mathbf{V}}_s^r\left(b^\Delta - \hat{b}^\Delta\right)\right]\mathrm{e}^{\text{-}j\phi_d} \tag{22}$$

Equations (21) and (22) show the effect of phase and capacitance errors on the first and second harmonic circulating currents. This information enables correction of the parameter errors by using current measurements as feedback.

B. Proposed Parameter Correction Method

Referring to (21) and (22), it can be observed that $\vec{\mathbf{I}}_2$ and $\vec{\mathbf{I}}_1$ can be forced to zero by adjusting the capacitance parameters, $\hat{b}^\Sigma$ and $\hat{b}^\Delta$, respectively. This procedure results in the elimination of the parameter errors. A feedback controller is proposed in this paper in order to achieve such parameter correction online. However, direct implementation of feedback control based on (21) and (22) results in difficulties because the dc gains of the resulting transfer functions, from $\hat{b}^\Sigma$ to $\vec{\mathbf{I}}_2$ and from $\hat{b}^\Delta$ to $\vec{\mathbf{I}}_1$, are dependent on the operating point of the system. This means that a controller designed for one operating point might lead to positive feedback at another point, causing instability. The proposed solution overcomes this challenge by transforming $\vec{\mathbf{I}}_2$ and $\vec{\mathbf{I}}_1$ such that the transfer function gains do not change sign over the whole operation range. Such a transformation is derived by first ignoring the time delays such that (21) and (22) simplify to (23) and (24).

$$-(R+jX_2)\vec{\mathbf{I}}_2 = j\left(b^\Sigma - \hat{b}^\Sigma\right)\vec{\mathbf{G}}_{20} - jG_{22}\vec{\mathbf{I}}_2 + j\vec{\mathbf{G}}_{21}\vec{\mathbf{I}}_1$$
$$\vec{\mathbf{G}}_{20} = \frac{1}{4\omega}\left[v_{cm}^r\vec{\mathbf{I}}_s - \frac{1}{2}i_c^0\vec{\mathbf{V}}_s^r\right]\vec{\mathbf{V}}_s^r \tag{23}$$

$$-(R+jX)\vec{\mathbf{I}}_1 = -j\left(b^\Delta - \hat{b}^\Delta\right)\vec{\mathbf{G}}_{10} - jG_{11}\vec{\mathbf{I}}_1 + j\vec{\mathbf{G}}_{12}\vec{\mathbf{I}}_2$$
$$\vec{\mathbf{G}}_{10} = \frac{1}{\omega}\left[\left(\frac{2}{3}(v_{cm}^r)^2 + \frac{1}{48}\|\vec{\mathbf{V}}_s^r\|^2\right)\vec{\mathbf{I}}_s - \frac{1}{2}v_{cm}^r i_{c0}\vec{\mathbf{V}}_s^r\right] \tag{24}$$

The proposed transformations are then given by (25).

$$\vec{\mathbf{T}}_2 = \frac{\vec{\mathbf{G}}_{20}^*}{\|\vec{\mathbf{G}}_{20}\|^2} \quad \text{and} \quad \vec{\mathbf{T}}_1 = \frac{\vec{\mathbf{G}}_{10}^*}{\|\vec{\mathbf{G}}_{10}\|^2} \tag{25}$$

TABLE III: Test system parameters.

Symbol	Value	Symbol	Value
S_b	60 kVA	C_{arm}	1110 µF
V_b^{dc}	700 V	$l_{dc} \times L_b^{dc}$	1.4 mH
V_b^{ac}	350 V	No. of SMs	18
k_{pw}	0.4	k_{pi}	0.1
k_{iw}	7.6	k_{ii}	6.9
T_w	10 ms	T_i	0.5 ms

Application of these transformations on both sides of (23) and (24) makes the coefficients of $\hat{b}^\Sigma$ and $\hat{b}^\Delta$ real constants irrespective of the operating point. Therefore, controllers designed for the transformed currents, $\vec{\mathbf{I}}_{2T} = \vec{\mathbf{T}}_2\vec{\mathbf{I}}_2$ and $\vec{\mathbf{I}}_{1T} = \vec{\mathbf{T}}_1\vec{\mathbf{I}}_1$, will be stable for the whole range of operating points without requiring re-tuning. The benefit of applying such a transformation will be shown by using simulation results. Since the effect is the same for both harmonic components, only $\vec{\mathbf{I}}_2$ will be covered in this section. Figure 3 compares the circulating current, $\vec{\mathbf{I}}_2$, with the transformed version, $\vec{\mathbf{I}}_{2T}$, under different operating points. The test was started with both the active and reactive power references set to 0.707 pu (OP1 in Fig. 3). Then, the active and reactive powers were reversed in polarity at $t = 7$ s, (OP2), and $t = 15$ s, (OP3), respectively. The currents are normalized by dividing them by their maximum value so that they can be plotted together. The shaded regions in the time plot and the diamond marks in the phasor plot show steady-state operating points. It is evident that both the real and imaginary parts of the circulating current ripple exhibit a sign change over the course of the simulation. This is particularly clear from the phasor plot where the current changes quadrant as the operating point changes. The change in quadrant makes the controllers designed for one operating point unstable at another. The transformed current ($\vec{\mathbf{I}}_{2T}$) does not exhibit the change in quadrant and, therefore, is suitable for the controllers. The movement of the transformed current within the third quadrant is due to the presence of delay error.

The same transformation helps in separating the effect of time delay from capacitance errors. This can be seen by applying $\vec{\mathbf{T}}_2$ and $\vec{\mathbf{T}}_1$ in the presence of time delay, i.e. to (21) and (22). Presence of the delay introduces an imaginary part to the coefficients of $\hat{b}^\Sigma$ and $\hat{b}^\Delta$ which in turn leads to an imaginary part in the transformed currents, $\vec{\mathbf{I}}_{2T}$ and $\vec{\mathbf{I}}_{1T}$. It can be shown, by linearizing (21) for small phase shift (around $\phi_d = 0$), that the imaginary part is proportional to the time delay and the corresponding transfer function gain does not change sign with operating point. The real part, on the other hand, is a function of both parameter errors. The same is true for the first harmonic part in (22). The controller implementation can be simplified if the phase error is corrected first. At the end of phase error correction, the resulting current is a function of only capacitance error as depicted in (23) and (24). Hence, the proposed implementation is performed in two steps as shown in Fig. 4.

The phase error can be corrected using the imaginary part of either $\vec{\mathbf{I}}_{2T}$ or $\vec{\mathbf{I}}_{1T}$. $\vec{\mathbf{I}}_{2T}$ is chosen in this paper because it is
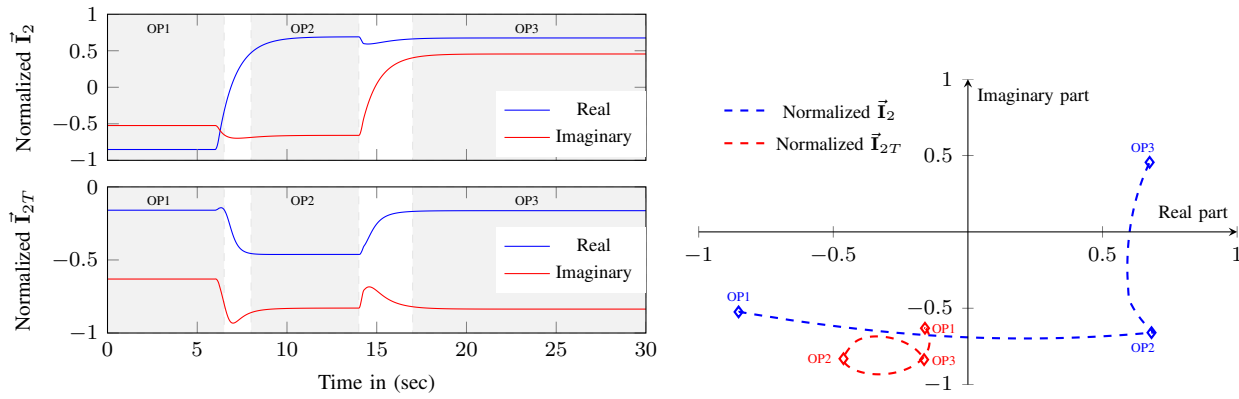
Fig. 3: Effect of the current transformation under different operating points: time plot (left) and phasor plot (right).
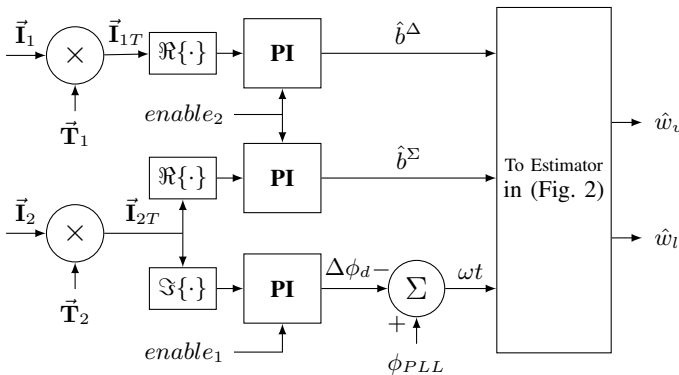

Fig. 4: Implementation of the proposed parameter correction method.

more sensitive to delay changes. Each controller is activated by the enable signals where the subscripts show the sequence of activation. ϕ_{PLL} is the angle obtained from a PLL or other means of acquiring phase angle of the grid voltage. The parameter correction controllers are not required to be always active. The enable signals can be generated by a supervisory logic controller that monitors peak value of the circulating current ripple. The controllers can be enabled when a pre-specified upper threshold is exceeded (e.g 0.1 pu) and then disabled once the parameters are corrected, which can be indicated by the ripple being below a lower threshold (e.g 0.01 pu). Another alternative is to run the parameter correction algorithm at regular intervals or during scheduled maintenance times. The parameter correction is implemented per-phase in order to identify each of the six arm capacitances individually. The phasors $\vec{I}_2$ and $\vec{I}_1$ are obtained by applying a method to extract phasors from single phase time domain signals, such as the one presented in [35]. The remaining phasors are obtained from a balanced three phase abc to $dq0$ transformation. The next section presents simulation and experimental results validating the proposed method.

V. SIMULATION AND EXPERIMENTAL RESULTS

The proposed scheme is verified by simulations and experimental tests using the test setup shown in Fig. 5. Both the ac and dc sides of the MMC are connected to a $200\,kVA$ grid emulator with a $10\,kHz$ bandwidth. The ac grid is emulated

by a voltage source behind an impedance while the dc side is represented by an ideal dc voltage source. The experiment was performed on three MMCs with 6, 12, and 18 levels. The results obtained from the three tests are similar, and hence, only the ones from the 18 level MMC will be presented in this paper. All the tests are performed at $500\,V$ dc, $225\,V$ ac peak, and $10\,kW$ active power being injected into the ac grid.

A. Test Cases

Table IV displays the test cases covered in this paper. The first case is a base case, where the parameter correction is disabled, and demonstrates the performance of the estimator, and the higher level controllers under normal conditions with nominal parameters. Case 2 deals with the correction of parameter errors, where the initial values for the estimator are obtained from the nameplates of the components (i.e. nominal values). This test case demonstrates the application of the proposed method for commissioning purpose, where the exact values of the parameters are not known. Cases 3 to 5 test how well the proposed method captures changes in arm capacitance. This was achieved by removing up to 2 capacitors from 4 (out of the 18) selected Sub-Modules of the three arms shown in Table IV. Each Sub-Module is composed of 6 capacitors connected in parallel. The arms are selected in such a way that the change introduced is unsymmetrical. The capacitor removals were done step-by-step, where the capacitors from Phase a upper arm were removed first, followed by Phase b lower arm, and finally, Phase c upper arm. The capacitors removed before the start of each test are not re-placed until the end of the last case. Therefore, at the start of case 5, a total of 21 capacitors were removed from the converter.

B. Base Case (Case 1)

This case presents the basic implementation of the estimator with nominal capacitances, and no time delay. In order to show the performance of the estimator during transients, a $20\,\%$ step change in the average arm voltage reference is applied at $10\,s$ and then reversed at $20\,s$. The simulation and experimental results for the base case are displayed side-by-side in Figs. 6 and 7. It can be seen from Fig. 6 that the estimator has a good
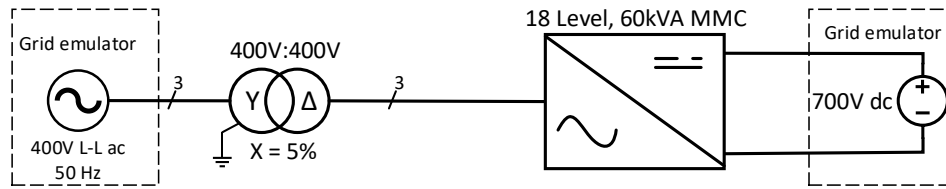
Fig. 5: Experimental test setup.

TABLE IV: Test Cases.

Case No.	Arm	No. of SMs Modified	No. of Caps removed out of 6				Change in arm Capacitance $(\Delta)^{**}$	Parameter correction
			SM1	SM2	SM3	SM4*		
1	-	0	0	0	0	0	0 %	No
2	-	0	0	0	0	0	0 %	Yes
3	Phase a upper	4	2	2	2	1	-8.6 %	Yes
4	Phase b lower	4	2	2	2	2	-10 %	Yes
5	Phase c upper	4	2	1	2	1	-7.2 %	Yes

*The remaining 14 Sub-Modules (SMs) are not modified in any of the cases.
**These values are approximations, calculated based on nominal values of the capacitors

performance in simulation. This is because the parameters are accurately known. The experimental results resemble the ones from the simulations confirming accuracy of the models used for simulation. The estimated and measured arm voltages from the experimental test in Fig. 6 seem to be well aligned. This, however, does not necessarily mean that the estimator is performing well because the measured arm voltage is different from the actual one due to distortion and delay in the measurement system. In simulation, the actual arm voltage is measured without distortion, and hence, good alignment means good performance. Therefore, the presence of circulating current ripple is used as an indicator of performance, where it is clear, (Fig. 7), that the estimator performs poorly in the experimental tests. It can be seen from Fig. 6 that the estimator performance slightly degrades during transient at 10 s. This is because the ac peaks and the dc signals are changing faster than what was specified in assumption **A.2**. As a consequence, the circulating current from the simulation displays ripple during transients as can be seen from the inset in Fig. 7. Magnitude of the resulting circulating current is negligible and only occurs during fast transients.

C. Parameter Error Correction

As identified in the base case, the converter parameters are different from their nominal values assumed by the estimator, which led to the circulating current ripple. In this section, the proposed method is used to remove this mismatch between the estimator and actual parameters. Figure 8 depicts the parameter correction controllers' output during the process of parameter correction. It can be seen that phase correction is applied first. Capacitance correction is enabled around $t = 10$ s, where the phase correction is expected to have reached steady-state. The values shown in Fig. 8 at the end of this test (at $t = 40$ s) are the mismatches between the parameters, the arm capacitances and ϕ_d, known to the estimator and those of the actual converter. Therefore, if the estimator parameters are adjusted by these values, the circulating current ripple can be eliminated. This

is shown in Fig. 9, where the magnitude of the circulating current ripple progressively decreases when the correction is activated. The phase adjustment experiences a deviation when the capacitance correction is enabled around 10 s. This is because of the removal of harmonic cross-coupling terms, derived in Section IV, which bias the relation between $\vec{\mathbf{I}}_{2T}$ and phase angle error. The remaining current ripple, at the end of the correction is measurement noise, harmonic distortion, and high frequency components due to switching of the Sub-Modules, which are not captured by average models. The upper and lower arm capacitance deviations (Fig. 8) for each phase are calculated from $\hat{b}^{\Sigma}$ and $\hat{b}^{\Delta}$ as given by (26).

$$\Delta c_u = \left(\frac{1}{c_a} \frac{1}{\hat{b}^{\Sigma} + \hat{b}^{\Delta}} - 1 \right) \times 100\%$$
$$\Delta c_l = \left(\frac{1}{c_a} \frac{1}{\hat{b}^{\Sigma} - \hat{b}^{\Delta}} - 1 \right) \times 100\% \tag{26}$$

where c_a is the nominal arm capacitance in per-unit. The controllers are not affected by the parameter correction since the correction scheme is disabled under normal operation. This can be asserted by observing the circulating current response to step changes in the arm energy, which is plotted in Fig. 10. This shows that, in comparison to Figs. 6 and 7, the correction reduces the current ripple without affecting the controller performance. This is an advantage compared to other approaches which use circulating current suppressors that are always active and can negatively interact with higher level controllers [13].

D. Change in Arm Capacitances

The parameter correction is also applied to cases 3 to 5, where the arm capacitances were modified. The resulting parameter adjustments are compared to those of case 2 in order to show how well the correction method copes with capacitance changes. Figure 11 depicts the upper and lower arm capacitance adjustments, which are calculated using (26). Each test was run similar to case 2 where the estimator is
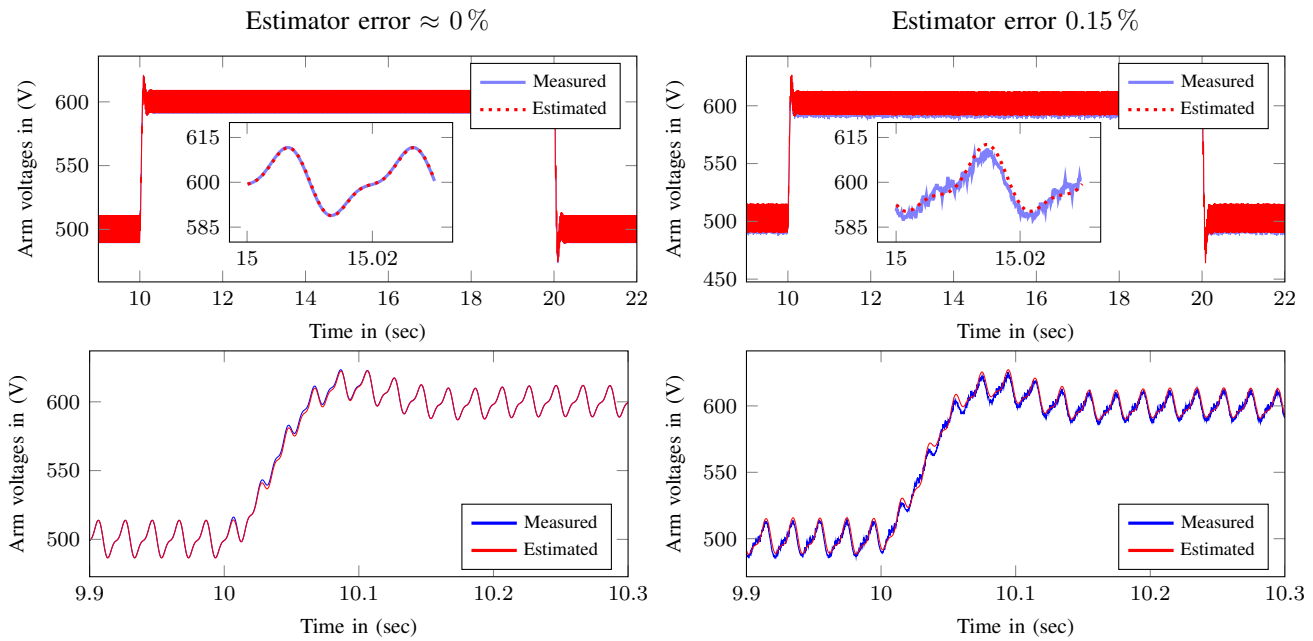
Fig. 6: Base case arm voltages in response to step in the arm energy reference and their zoomed versions in the second row: simulation (left) and experimental (right).
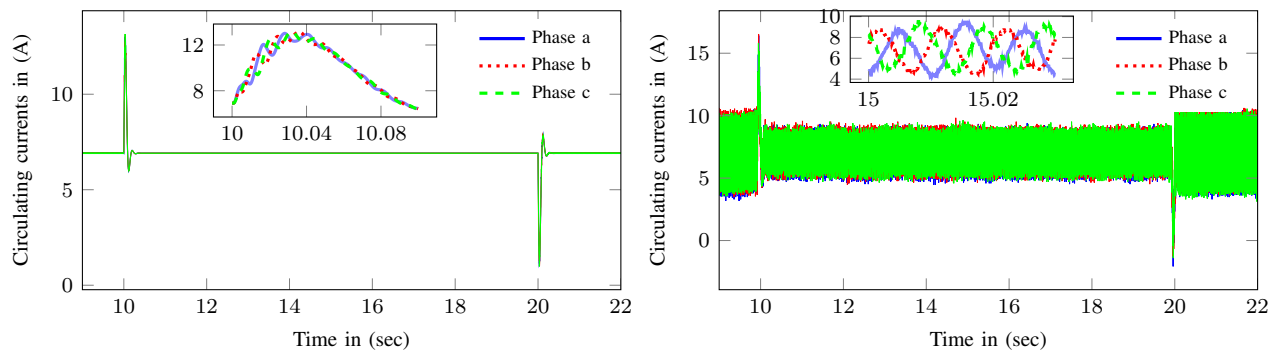

Fig. 7: Base case circulating currents in response to step in the arm energy reference: simulation (left) and experimental (right).

started with nominal values of the arm capacitances and no delay. Only the test cases relevant to the respective phases are shown in the figure in order to provide clear comparison of the deviations. For instance, since Phase a upper arm is modified in case 3, the result in Fig. 11 compares case 3 to case 2 in order to show the change in capacitance. The unmodified arm in the same phase is also displayed to show that it is not affected by the removal of the capacitors. It can be seen that the proposed method correctly captures the capacitance modifications. Figure 11 also shows the percentage difference between the adjustments of case 2 and cases 3 to 5, where it can be seen that the adjustments are in close agreement with the values shown in Table IV. The mismatch between the deviations in Table IV and Fig. 11 can be attributed to two reasons: 1) the capacitance tolerances, which change the deviations in Table IV, and 2) the presence of measurement noise, which prevents ideal operation of the correction method. The noise problem can be overcome by running the correction at higher currents where signal-to-noise ratio is higher. It should be noted, however, that the method performs well in

removing the ripples, even in the presence of noise. The other option to minimize the impact of noise is to apply filtering to the current measurements and tune the correction controllers to be slower.

VI. DISCUSSION AND CONCLUSION

This paper presents a complete approach for implementing compensated modulation without accurate knowledge of system parameters. Parameter errors lead to two types of problems: deviation of the average component from the desired one, and increase in the circulating current ripple. This paper addresses these two separately. As a first part, the average part is decoupled from the errors by using the measured average value. This is acceptable because the average part is assumed to change slowly enough that it is not affected by the measurement system. Additionally, the average part is controlled in closed-loop in order to provide good dynamic performance and disturbance rejection. The second part is on correction of parameter errors to reduce or eliminate the circulating current ripple.
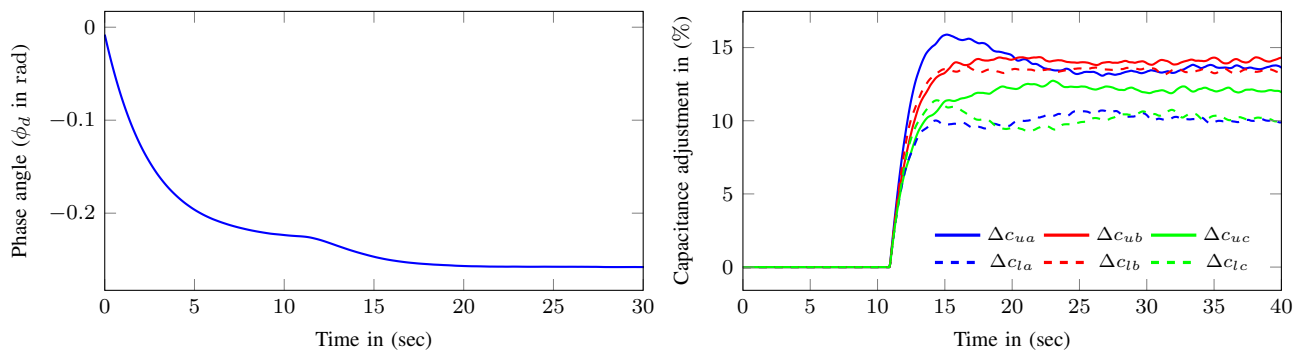
Fig. 8: Parameters during the process of correction (Case 2): phase angle (left) and capacitance (right).
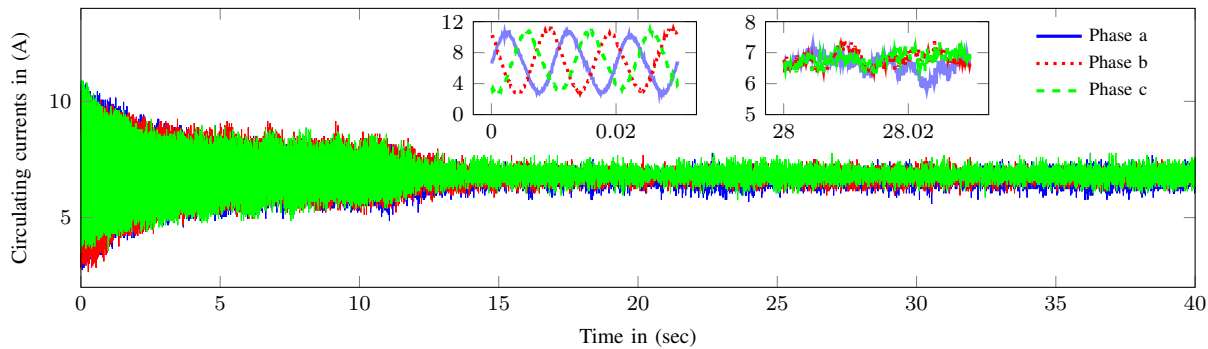

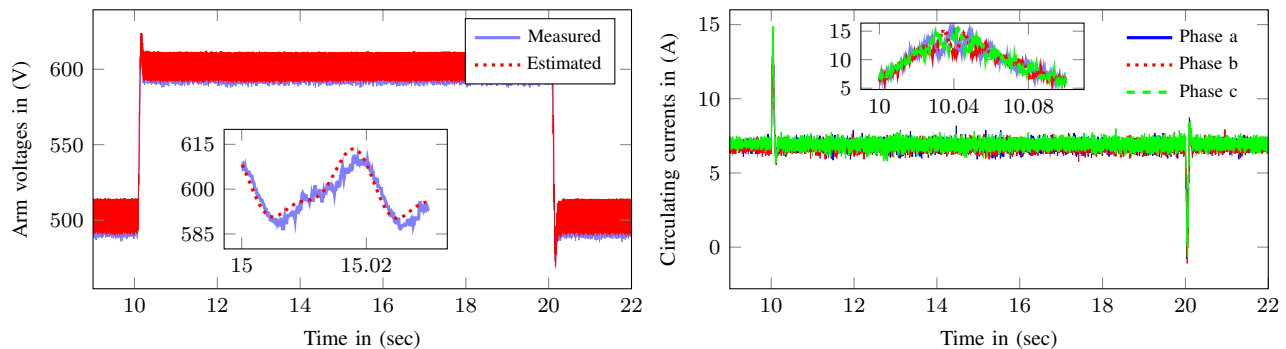Fig. 9: Circulating current during parameter correction (experimental).

Fig. 10: Arm voltage and circulating current after parameter error correction (experimental).

The parameters considered in this paper are the arm capacitance and time delay between the controller and the converter. The detailed derivation has shown that these quantities are related to the first and second harmonic ripples in the circulating current. A transformation is applied to the second harmonic current in order to make its imaginary part, in phasor domain, a function of only the phase error. This enables a two-step correction of the two errors: phase correction using the imaginary part of the second harmonic, followed by sum and difference capacitance corrections using the real parts of the second and first harmonic phasors, respectively. It can be observed that despite its rather long analytic derivation, the final result is simple and easy to implement (Fig. 4). The corrections are implemented using two PI controllers per leg that are enabled on-demand. Further, the controllers are designed to be slower than higher level controllers, which results in time-scale separation. This enables removal of the circulating current ripple without potential negative interactions with the higher level controllers.

The proposed method has been tested using both simulation and experimental tests with a strong correlation between the two results. The experimental tests have shown that the method can work in cases that are not ideal where the number of modules is as low as 18. The tests have also demonstrated that the method works well in the presence of noise and unsymmetrical capacitance changes. In summary, the proposed method gives a complete solution for implementing compensated modulation under changing system parameters. Moreover, the application of the method is not limited to the correction of parameter changes due to environmental conditions; it can also be used to identify the parameters during commissioning where they are not accurately known.
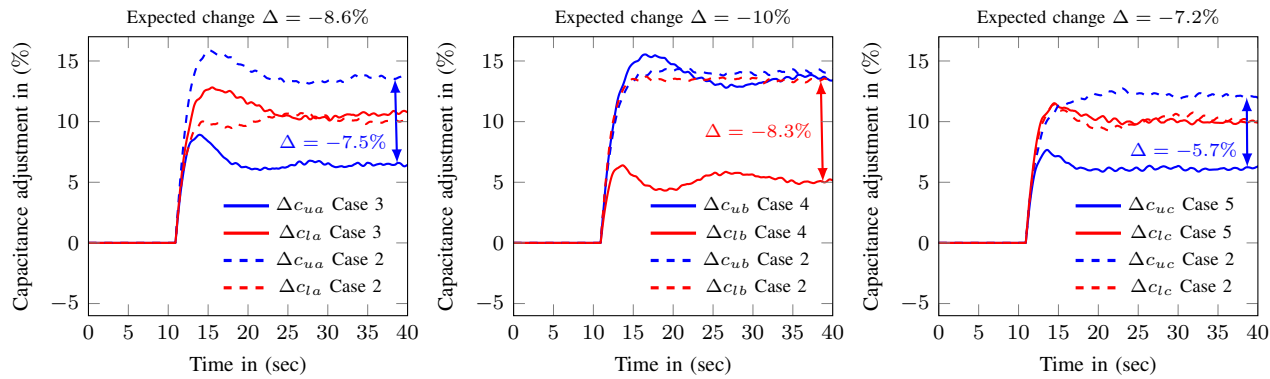
Fig. 11: Capacitance adjustments before and after capacitor removals: Phase *a* (left), Phase *b* (middle), and Phase *c* (right).

REFERENCES

[1] A. Lesnicar and R. Marquardt, "An innovative modular multilevel converter topology suitable for a wide power range," in *2003 IEEE Bologna Power Tech Conference Proceedings,*, vol. 3, Jun. 2003, pp. 6 pp. Vol.3–.

[2] H. Akagi, "Classification, Terminology, and Application of the Modular Multilevel Cascade Converter (MMCC)," *IEEE Trans. Power Electron.*, vol. 26, no. 11, pp. 3119–3130, Nov. 2011.

[3] S. Debnath, J. Qin, B. Bahrani, M. Saeedifard, and P. Barbosa, "Operation, Control, and Applications of the Modular Multilevel Converter: A Review," *IEEE Trans. Power Electron.*, vol. 30, no. 1, pp. 37–53, Jan. 2015.

[4] M. A. Perez, S. Bernet, J. Rodriguez, S. Kouro, and R. Lizana, "Circuit Topologies, Modeling, Control Schemes, and Applications of Modular Multilevel Converters," *IEEE Trans. Power Electron.*, vol. 30, no. 1, pp. 4–17, Jan. 2015.

[5] M. Barnes and A. Beddard, "Voltage Source Converter HVDC Links – The State of the Art and Issues Going Forward," *Energy Procedia*, vol. 24, pp. 108–122, Jan. 2012.

[6] L. Ängquist, A. Haider, H. P. Nee, and H. Jiang, "Open-loop approach to control a Modular Multilevel Frequency Converter," in *Proc. 2011-14th European Conf. Power Electronics and Applications (EPE 2011)*, Aug. 2011, pp. 1–10.

[7] K. Sharifabadi, L. Harnefors, H.-P. Nee, S. Norrga, and R. Teodorescu, *Design, Control and Application of Modular Multilevel Converters for HVDC Transmission Systems*. Chichester, UK: John Wiley & Sons, Ltd, Aug. 2016.

[8] M. Sleiman, K. Al-Haddad, H. F. Blanchette, and H. Y. Kanaan, "Insertion Index Generation Method Using Available Leg-Average Voltage to Control Modular Multilevel Converters," *IEEE Trans. Ind. Electron.*, vol. PP, no. 99, pp. 1–11, 2017.

[9] A. A. Taffese, E. Tedeschi, and E. de Jong, "Arm voltage estimation method for compensated modulation of modular multilevel converters," in *2017 IEEE Manchester PowerTech*, Jun. 2017, pp. 1–6.

[10] D. Siemaszko, A. Antonopoulos, K. Ilves, M. Vasiladiotis, L. Ängquist, and H. P. Nee, "Evaluation of control and modulation methods for modular multilevel converters," in *The 2010 International Power Electronics Conference - ECCE ASIA -*, Jun. 2010, pp. 746–753.

[11] G. Bergna-Diaz, J. Freytes, X. Guillaud, S. D'Arco, and J. A. Suul, "Generalized Voltage-based State-Space Modelling of Modular Multilevel Converters with Constant Equilibrium in Steady-State," *IEEE J. Emerg. Sel. Top. Power Electron.*, pp. 1–18, 2018.

[12] A. Antonopoulos, L. Angquist, and H. P. Nee, "On dynamics and voltage control of the Modular Multilevel Converter," in *2009 13th European Conference on Power Electronics and Applications*, Sep. 2009, pp. 1–10.

[13] J. Freytes, G. Bergna, J. A. Suul, S. D'Arco, F. Gruson, F. Colas, H. Saad, and X. Guillaud, "Improving Small-Signal Stability of an MMC with CCSC by Control of the Internally Stored Energy," *IEEE Trans. Power Deliv.*, vol. PP, no. 99, pp. 1–10, 2017.

[14] B. Bahrani, S. Debnath, and M. Saeedifard, "Circulating Current Suppression of the Modular Multilevel Converter in a Double-Frequency Rotating Reference Frame," *IEEE Trans. Power Electron.*, vol. 31, no. 1, pp. 783–792, Jan. 2016.

[15] X. She, A. Huang, X. Ni, and R. Burgos, "AC circulating currents suppression in modular multilevel converter," in *IECON 2012 - 38th Annual Conference on IEEE Industrial Electronics Society*, Oct. 2012, pp. 191–196.

[16] Q. Tu, Z. Xu, and L. Xu, "Reduced Switching-Frequency Modulation and Circulating Current Suppression for Modular Multilevel Converters," *IEEE Trans. Power Deliv.*, vol. 26, no. 3, pp. 2009–2017, Jul. 2011.

[17] Z. Li, P. Wang, Z. Chu, H. Zhu, Y. Luo, and Y. Li, "An Inner Current Suppressing Method for Modular Multilevel Converters," *IEEE Trans. Power Electron.*, vol. 28, no. 11, pp. 4873–4879, Nov. 2013.

[18] A. a. J. Far and D. Jovcic, "Circulating current suppression control dynamics and impact on MMC converter dynamics," in *2015 IEEE Eindhoven PowerTech*, Jun. 2015, pp. 1–6.

[19] L. Ängquist, A. Antonopoulos, D. Siemaszko, K. Ilves, M. Vasiladiotis, and H. P. Nee, "Inner control of Modular Multilevel Converters - An approach using open-loop estimation of stored energy," in *The 2010 International Power Electronics Conference - ECCE ASIA -*, Jun. 2010, pp. 1579–1585.

[20] L. Harnefors, A. Antonopoulos, K. Ilves, and H. P. Nee, "Global Asymptotic Stability of Current-Controlled Modular Multilevel Converters," *IEEE Trans. Power Electron.*, vol. 30, no. 1, pp. 249–258, Jan. 2015.

[21] A. Antonopoulos, L. Ängquist, L. Harnefors, K. Ilves, and H. P. Nee, "Global Asymptotic Stability of Modular Multilevel Converters," *IEEE Trans. Ind. Electron.*, vol. 61, no. 2, pp. 603–612, Feb. 2014.

[22] C. S. Kulkarni, J. R. Celaya, G. Biswas, and K. Goebel, "Accelerated aging experiments for capacitor health monitoring and prognostics," in *2012 IEEE AUTOTESTCON Proceedings*, Sep. 2012, pp. 356–361.

[23] Y.-J. Jo, T. H. Nguyen, and D.-C. Lee, "Capacitance Estimation of the Submodule Capacitors in Modular Multilevel Converters for HVDC Applications," *J. Power Electron.*, vol. 16, no. 5, pp. 1752–1762, 2016.

[24] H. R. Wickramasinghe, G. Konstantinou, S. Ceballos, and J. Pou, "Alternate Arm Converter Energy Balancing under Parameter Variation," *IEEE Trans. Power Electron.*, pp. 1–1, 2018.

[25] L. Harnefors, A. Antonopoulos, S. Norrga, L. Angquist, and H. P. Nee, "Dynamic Analysis of Modular Multilevel Converters," *IEEE Trans. Ind. Electron.*, vol. 60, no. 7, pp. 2526–2537, Jul. 2013.

[26] U. N. Gnanarathna, A. M. Gole, and R. P. Jayasinghe, "Efficient Modeling of Modular Multilevel HVDC Converters (MMC) on Electromagnetic Transient Simulation Programs," *IEEE Trans. Power Deliv.*, vol. 26, no. 1, pp. 316–324, Jan. 2011.

[27] H. Saad, J. Peralta, S. Dennetière, J. Mahseredjian, J. Jatskevich, J. A. Martinez, A. Davoudi, M. Saeedifard, V. Sood, X. Wang, J. Cano, and A. Mehrizi-Sani, "Dynamic Averaged and Simplified Models for MMC-Based HVDC Transmission Systems," *IEEE Trans. Power Deliv.*, vol. 28, no. 3, pp. 1723–1730, Jul. 2013.

[28] G. Bergna-Diaz, J. A. Suul, and S. D'Arco, "Energy-Based State-Space Representation of Modular Multilevel Converters with a Constant Equi-

This article has been accepted for publication in a future issue of this journal, but has not been fully edited. Content may change prior to final publication. Citation information: DOI 10.1109/TPEL.2019.2907178, IEEE Transactions on Power Electronics

13

librium Point in Steady-State Operation," *IEEE Trans. Power Electron.*, vol. PP, no. 99, pp. 1–19, 2017.

[29] S. S. Khan and E. Tedeschi, "Modeling of MMC for Fast and Accurate Simulation of Electromagnetic Transients: A Review," vol. 10, no. 8, p. 1161, Aug. 2017.

[30] A. Ferreira, C. Collados, O. Gomis-Bellmunt, and M. Teixido, "Modular multilevel converter electrical circuit model for HVdc applications," in *2015 17th European Conference on Power Electronics and Applications (EPE'15 ECCE-Europe)*, Sep. 2015, pp. 1–10.

[31] G. Bergna Diaz, J. A. Suul, and S. D'Arco, "Small-signal state-space modeling of modular multilevel converters for system stability analysis," in *Energy Conversion Congress and Exposition (ECCE), 2015 IEEE*. IEEE, 2015, pp. 5822–5829.

[32] M. Vasiladiotis, N. Cherix, and A. Rufer, "Accurate Capacitor Volt-age Ripple Estimation and Current Control Considerations for Grid-Connected Modular Multilevel Converters," *IEEE Trans. Power Electron.*, vol. 29, no. 9, pp. 4568–4579, Sep. 2014.

[33] "IEEE Recommended Practice and Requirements for Harmonic Control in Electric Power Systems," *IEEE Std 519-2014 Revis. IEEE Std 519-1992*, pp. 1–29, Jun. 2014.

[34] J. W. Umland and M. Safiuddin, "Magnitude and symmetric optimum criterion for the design of linear control systems: What is it and how does it compare with the others?" *IEEE Trans. Ind. Appl.*, vol. 26, no. 3, pp. 489–497, May 1990.

[35] L. Angquist and C. Gama, "Damping algorithm based on phasor estimation," in *2001 IEEE Power Engineering Society Winter Meeting. Conference Proceedings (Cat. No.01CH37194)*, vol. 3, 2001, pp. 1160–1165 vol.3.